

High-fidelity state detection and tomography of a single-ion Zeeman qubit

This article has been downloaded from IOPscience. Please scroll down to see the full text article.

2011 New J. Phys. 13 073027

(<http://iopscience.iop.org/1367-2630/13/7/073027>)

View [the table of contents for this issue](#), or go to the [journal homepage](#) for more

Download details:

IP Address: 132.77.4.129

The article was downloaded on 21/07/2011 at 11:39

Please note that [terms and conditions apply](#).

High-fidelity state detection and tomography of a single-ion Zeeman qubit

A Keselman, Y Glickman, N Akerman, S Kotler and R Ozeri¹

Physics of Complex Systems, The Weizmann Institute of Science,
Rehovot 76100, Israel

E-mail: ozeri@weizmann.ac.il

New Journal of Physics **13** (2011) 073027 (17pp)

Received 26 March 2011

Published 21 July 2011

Online at <http://www.njp.org/>

doi:10.1088/1367-2630/13/7/073027

Abstract. We demonstrate high-fidelity Zeeman qubit state detection in a single trapped $^{88}\text{Sr}^+$ ion. Qubit readout is performed by shelving one of the qubit states to a metastable level using a narrow linewidth diode laser at 674 nm, followed by state-selective fluorescence detection. The average fidelity reached for the readout of the qubit state is 0.9989(1). We then measure the fidelity of state tomography, averaged over all possible single-qubit states, which is 0.9979(2). We also fully characterize the detection process using quantum process tomography. This readout fidelity is compatible with recent estimates of the detection error threshold required for fault-tolerant computation, whereas high-fidelity state tomography opens the way for high-precision quantum process tomography.

¹ Author to whom any correspondence should be addressed.

Contents

1. Introduction	2
2. Experimental setup	3
3. State discrimination	5
4. Experimental sequence	7
5. State detection results	8
6. Error budget	8
6.1. Initialization error	9
6.2. Electron shelving error	10
6.3. Error summary	12
7. High-fidelity quantum-state tomography	13
8. Summary	16
Acknowledgments	16
References	16

1. Introduction

One of the basic requirements for implementing a physical qubit is the ability to faithfully measure its state [1]. Furthermore, qubit state detection must be performed with high fidelity to reach fault-tolerant quantum computation. The exact detection error threshold required depends on many factors; however, under quite general assumptions error values of the order of 10^{-2} – 10^{-4} were estimated [2]. Another important use of high-fidelity state detection is precision process tomography for studying different quantum processes.

Trapped ion qubits are a promising candidate system for physically realizing a quantum computer, and serve as a convenient test ground for studying fundamental quantum dynamics. Ion species used for this purpose typically have a single electron in their valence shell and the two qubit states are encoded in two energy levels of the valence electron. The state detection methods used to date rely on state-selective fluorescence. Here, photons are scattered from a laser that is resonant with a transition from one of the qubit states to a short-lived excited state, whereas transitions from the other qubit state are largely off-resonance. State inference is then based on the detected photon statistics [3]. To this end, qubit choices with a large energy separation are advantageous.

For optical qubits, in which the two qubit states are separated by an optical transition, state detection fidelity as high as 0.9999 was demonstrated using state-selective fluorescence and accounting for photon arrival times [4, 5]. Another detection scheme, using repetitive quantum non-demolition measurements on an ancilla ion-qubit, was shown to give a fidelity of 0.9994 [6]. Optical qubits, however, have the disadvantage of an excited state lifetime of the order of 1 s, depending on the exact ion species used. Furthermore, the linewidth of even ultra-stable optical local oscillators, i.e. frequency-stabilized lasers, would limit the dephasing time of an optical qubit.

Qubits that are encoded into a pair of levels in the electronic ground state, in which the two qubit levels are split, either by the Zeeman effect or the hyperfine interaction, by radio-frequency (RF) transitions, have practically an infinite lifetime, as well as a very long coherence time [7].

Hyperfine qubit levels are typically separated by frequencies in the GHz range. State detection for this type of qubit can still be implemented by direct state-selective fluorescence, since the typical linewidth of electric-dipole transitions is two orders of magnitude smaller. Here, off-resonance scattering normally limits state detection fidelity to below 0.995 [8–10]. The use of ancilla qubits can, in principle, increase the detection fidelity of a hyperfine ion-qubit [11]. In ion species that have low-lying metastable levels, one of the qubit states can be shelved to a metastable level prior to detection. Here, detection fidelity is similar to that of an optical qubit with an additional error introduced by the state shelving process. Using state-selective optical pumping for shelving, a hyperfine ion-qubit measurement fidelity as high as 0.9977 was demonstrated [4].

Ion-qubits that are encoded into a pair of Zeeman split levels pose the hardest state-measurement challenge. This is because the frequency separation between the qubit levels is typically in the MHz range and is comparable to the spectral linewidth of electric-dipole transitions used for state-selective fluorescence. Since direct state-selective fluorescence is impossible, Zeeman qubits can be read out only by state mapping onto a hyperfine ancilla qubit [6] or by shelving one of the qubit states onto a metastable level. However, the fidelity of state shelving in a Zeeman qubit using optical pumping is limited due to the strong coupling of the shelving light to the other qubit state [12]. Thus, the only way to state-selectively shelve a Zeeman qubit with high fidelity is by using a narrow-linewidth laser. Although there have been several reports on detecting a Zeeman qubit with shelving via a narrow-linewidth laser, with typical fidelities below 0.996 [13, 14], to our knowledge there has not been a systematic study of the measurement error and limitations in this kind of qubit.

Here, we demonstrate the readout of a single-ion Zeeman qubit with a fidelity of 0.9989(1). Spin state detection is performed via electron shelving with a narrow-linewidth diode laser, followed by state-selective fluorescence. We analyze the different fundamental sources as well as technical sources of measurement error in detail. In contrast to the work of Myerson *et al*, where high-fidelity distinguishability was demonstrated between different level manifolds rather than qubit states, here we demonstrate high-fidelity qubit state detection. Qubit rotations can therefore be used to carry out measurements in different basis states. We thus use the high-fidelity state detection of our qubit to demonstrate high-fidelity state tomography [15]. Here, we measure the fidelity of quantum state tomography averaged over all possible single-qubit states and also fully characterize the detection process using quantum process tomography.

2. Experimental setup

We trap a single $^{88}\text{Sr}^+$ ion in a linear RF Paul trap. The trapping potential is well approximated as harmonic with a secular axial frequency of $\omega_{\text{ax}} = (2\pi)1.09$ MHz and two nearly degenerate radial frequencies of $\omega_r = (2\pi)2.5$ MHz. A scheme of the relevant energy levels in $^{88}\text{Sr}^+$ is shown in figure 1. The $|\uparrow\rangle$ and $|\downarrow\rangle$ qubit states are encoded in the $5S_{1/2,+1/2}$ and $5S_{1/2,-1/2}$ spin states, respectively. A magnetic field of 0.477 mT splits the two qubit levels by a frequency $\omega_0 = (2\pi)13.366$ MHz.

An oscillating magnetic field, perpendicular to the quantization axis, is generated by a current, oscillating at $\omega_0/(2\pi)$, through an electrode positioned 2 mm from the ion, resulting in coherent coupling between the two qubit levels. Zeeman qubit coherent rotations are therefore generated by oscillating current pulses.

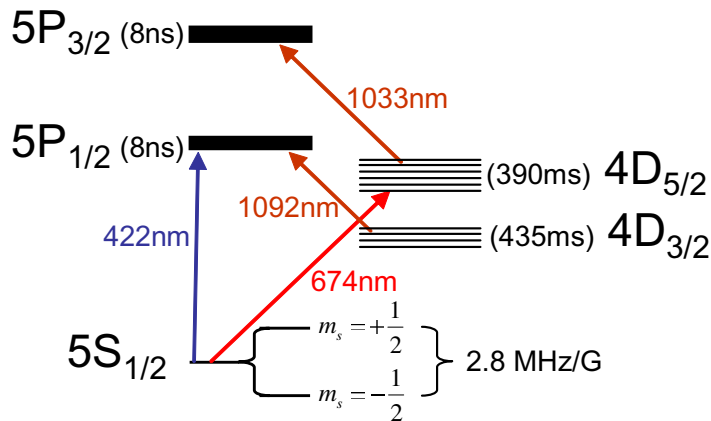


Figure 1. Energy levels scheme of the single valence electron of the $^{88}\text{Sr}^+$ ion. The $|\uparrow\rangle$ and $|\downarrow\rangle$ qubit states are encoded in the two, Zeeman-split, spin-1/2 states of the $S_{1/2}$ ground level. Energy level lifetimes are written next to their spectroscopic notation. Laser light at 422 nm performs laser cooling and state-selective fluorescence. Lasers at 1092 and 1033 nm pump out population from the metastable $D_{3/2}$ and $D_{5/2}$ levels, respectively. A 674 nm narrow linewidth diode laser shelves the electron from the qubit levels to levels in the $D_{5/2}$ manifold.

In the first part of state detection, the electron is shelved from the $|\uparrow\rangle$ state to one of the $D_{5/2}$, Zeeman-split, levels using a narrow-linewidth, 674 nm, external cavity diode laser. The diode laser is stabilized to a high-finesse (10^5), ultra-low expansion glass, reference cavity. Residual frequency noise of the laser has three dominant spectral features. Firstly, slow thermal drifts of the cavity result in drifts of the laser frequency with a typical magnitude of 10 Hz/S. The atomic resonance frequency is scanned every 2 min to correct for this drift. Secondly, intermediate frequency noise results in a laser line half-width of 70 Hz over several seconds, estimated in a Ramsey spectroscopy experiment [16]. The third spectral feature results from fast frequency noise that is unsuppressed, or even slightly enhanced, by our frequency servo system. This spectral feature is often referred to as the servo bump. Our servo bumps are centered around 700 kHz on both sides of the carrier, having a width of ~ 300 kHz, and contain an estimated $< 5\%$ of the optical power. A detailed discussion of our narrow linewidth diode laser system is given in [17]. In this experiment, the direction of 674 nm laser light propagation relative to the Zeeman splitting magnetic field direction limits the allowed transitions between $S_{1/2}$ and $D_{5/2}$ manifolds to $\Delta m = \pm 1$ transitions.

Electron shelving is followed by state-selective fluorescence detection on the $S_{1/2} \rightarrow P_{1/2}$ transition at 422 nm. Photons that are scattered in a direction perpendicular to the 422 nm laser beam and the magnetic field are collected by an imaging system ($\text{NA} = 0.31$) and are detected with a photo multiplier tube (PMT). State inference relies on the detected photon statistics. Qualitatively, a small number of detected photons implies that the ion qubit started in the $|\uparrow\rangle$ state and was shelved to the non-fluorescing $D_{5/2}$ level, whereas a large number of detected photons implies that the ion qubit started in the $|\downarrow\rangle$ state and therefore was not shelved and remained at the fluorescing $S_{1/2}$ level.

3. State discrimination

Following electron shelving, the number of photons n detected by the PMT during a given detection time, t_{det} , is a random variable. This random variable is denoted by n_b if the ion is in the fluorescing (bright) state $S_{1/2}$ and by n_d if the ion is in the non-fluorescing (dark) state $D_{5/2}$. Photon detection events, which occur when the ion is in the dark state, are primarily due to scattering of the laser beam from trap surfaces. The fidelity of state discrimination is compromised by the overlap of the probability distribution functions (PDFs) of these two random variables. State inference can be performed by introducing a threshold value for the number of photons detected, n_{th} . If the number of photons detected is greater (smaller) than this threshold, $n > (<=)n_{\text{th}}$, then we can infer that the ion is in the bright (dark) state. Given the PDFs for n_b and n_d , the errors in detecting the bright and dark states are $\epsilon_b = p_b(n \leq n_{\text{th}})$ and $\epsilon_d = p_d(n > n_{\text{th}})$, respectively. We want to find the parameters t_{det} and n_{th} that minimize the mean error

$$\epsilon = \frac{\epsilon_b + \epsilon_d}{2} = \frac{p_b(n \leq n_{\text{th}}) + p_d(n > n_{\text{th}})}{2}. \quad (1)$$

The detection fidelity is then given by $F = 1 - \epsilon$. If the lifetime of the $D_{5/2}$ level had been infinite, the random variables n_b and n_d would follow two Poisson distributions. Given photon detection rates R_b and R_d in the bright and dark states, respectively, and a detection time, t_{det} , the means of these distributions would be given by $\bar{n}_{b,d} = R_{b,d} t_{\text{det}}$. Here, the longer the detection time, the smaller the overlap between the two PDFs and therefore also the detection error. However, the finite lifetime, $\tau_{D_{5/2}}$, of the $D_{5/2}$ level introduces a correction to the PDF for n_d , since there is a finite probability for the ion to decay during the detection. Upon decay, the photon detection rate becomes R_b . At a detection time much shorter than the $D_{5/2}$ lifetime, $t_{\text{det}} \ll \tau_{D_{5/2}}$, the PDFs for n_b and n_d are given by [18]

$$p_b(n) = \text{Pois}(n, \bar{n}_b), \quad (2a)$$

$$p_d(n) = \left(1 - \frac{t_{\text{det}}}{\tau}\right) \text{Pois}(n, \bar{n}_d) + \frac{t_{\text{det}}}{\tau} \frac{\Gamma(\bar{n}_b, n+1) - \Gamma(\bar{n}_d, n+1)}{\bar{n}_b - \bar{n}_d}, \quad (2b)$$

respectively. Here, $\text{Pois}(n, \bar{n})$ denotes the probability of detecting n photons for a Poisson distribution with a mean \bar{n} , and $\Gamma(x, a) = \frac{1}{\Gamma(a)} \int_0^x e^{-t} t^{a-1} dt$ is the incomplete gamma function. The two PDFs are denoted by the blue and red curves in figure 2, for our measured photon detection rates $R_b = 73.5$ kHz and $R_d = 1.75$ kHz, a detection time of $t_{\text{det}} = 285 \mu\text{s}$ and the known $D_{5/2}$ level lifetime, $\tau_{D_{5/2}} = 390$ ms [19].

When the detection time is increased, the overlap between the two functions initially decreases owing to the larger spacing between the two Poisson peaks, but eventually increases owing to the growing tail of the dark distribution. Hence, an optimal detection time and a threshold number of photons exist such that the error in state discrimination is minimal. Figure 3(a) shows a contour plot for ϵ , as a function of the detection time t_{det} and the threshold on the number of photons n_{th} , for the same R_b , R_d and $\tau_{D_{5/2}}$ values as those used in figure 2. A minimal error of $\epsilon \simeq 2.9 \times 10^{-4}$ is calculated at a detection time of $t_{\text{det}} = 280 \mu\text{s}$ and an $n_{\text{th}} = 5$ threshold value for the number of detected photons.

The actual distributions measured in the experiment are also affected by the state preparation error, and an error resulting from an imperfect shelving of the ion to the metastable state. State preparation errors, $\epsilon_{\downarrow, \text{init}}$ and $\epsilon_{\uparrow, \text{init}}$ for the $|\downarrow\rangle$ and $|\uparrow\rangle$ states, respectively, are given

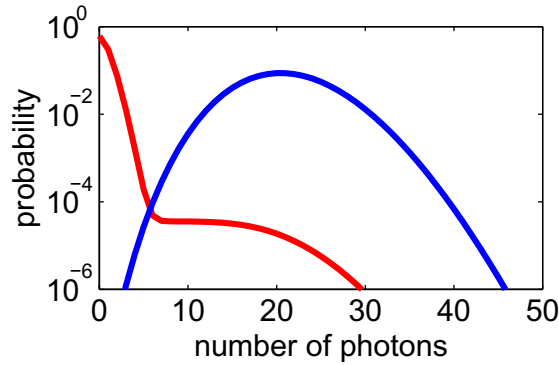


Figure 2. Theoretical probability density functions for the number of detected photons in the bright (blue line) and dark (red line) states, given in equations (2a) and (2b), using our measured photon detection rates $R_b = 73.5$ kHz and $R_d = 1.75$ kHz, a detection time of $t_{\text{det}} = 285$ μs and the known $D_{5/2}$ level lifetime, $\tau_{D_{5/2}} = 390$ ms.

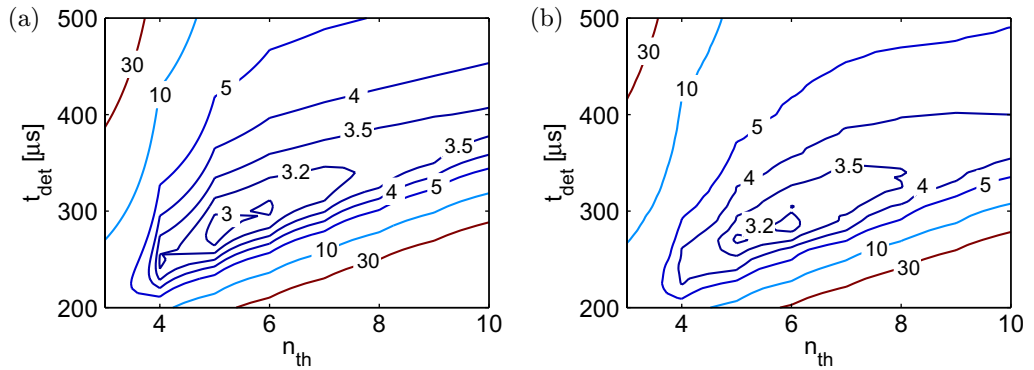


Figure 3. State discrimination error as a function of the detection time t_{det} and the threshold on the number of photons n_{th} . (a) Theoretical estimation obtained using equations (2a) and (2b). The measured photon detection rates of $R_b = 73.5$ kHz and $R_d = 1.75$ kHz are assumed, as well as the known lifetime of the $D_{5/2}$ level, $\tau_{D_{5/2}} = 390$ ms [19]. A minimal error of $\epsilon = 2.9 \times 10^{-4}$ is calculated at a detection time of $t_{\text{det}} = 280$ μs and an $n_{\text{th}} = 5$ threshold value for the number of detected photons. (b) Experimental results. Here the mean initialization and shelving error of 8×10^{-4} was subtracted. A minimal error of $\epsilon = 3(1) \times 10^{-4}$ is measured at a detection time of $t_{\text{det}} = 285$ μs and a threshold value for the number of photons of $n_{\text{th}} = 6$. The theoretical model and our data are seen to be in relatively good agreement.

by the fraction of experiments in which the ion was initialized in the wrong state. The shelving error for the $|\uparrow\rangle$ state, $\epsilon_{\uparrow, \text{shelving}}$, is the probability that the ion remained at the $S_{1/2}$ level after shelving was performed. For the $|\downarrow\rangle$ state, $\epsilon_{\downarrow, \text{shelving}}$ is the probability that the ion was shelved to the $D_{5/2}$ level due to off-resonant light. Neglecting terms that are second order in the different

errors, the resulting PDFs for the $|\downarrow\rangle$ and $|\uparrow\rangle$ states are given by [18]

$$\tilde{p}_\downarrow(n) \simeq (1 - \epsilon_{\downarrow,\text{tot}}) \text{Poiss}(n, \bar{n}_b) + \epsilon_{\downarrow,\text{tot}} \text{Poiss}(n, \bar{n}_d), \quad (3a)$$

$$\tilde{p}_\uparrow(n) \simeq \left(1 - \epsilon_{\uparrow,\text{tot}} - \frac{t_{\text{det}}}{\tau}\right) \text{Poiss}(n, \bar{n}_d) + \frac{t_{\text{det}}}{\tau} \frac{\Gamma(\bar{n}_b, n+1) - \Gamma(\bar{n}_d, n+1)}{\bar{n}_b - \bar{n}_d} + \epsilon_{\uparrow,\text{tot}} \text{Poiss}(n, \bar{n}_b). \quad (3b)$$

Note that only the sum of the initialization error and the shelving error appears: $\epsilon_{\downarrow/\uparrow,\text{tot}} = \epsilon_{\downarrow/\uparrow,\text{init}} + \epsilon_{\downarrow/\uparrow,\text{shelving}}$. This prevents us from distinguishing the state preparation error from the shelving error. The total mean detection error

$$\tilde{\epsilon} = \frac{\tilde{\epsilon}_\downarrow + \tilde{\epsilon}_\uparrow}{2} = \frac{\tilde{p}_\downarrow(n \leq n_{\text{th}}) + \tilde{p}_\uparrow(n > n_{\text{th}})}{2} \quad (4)$$

can be related to the error ϵ resulting from the finite lifetime of the metastable level alone, obtained before

$$\tilde{\epsilon} = \epsilon + \frac{\epsilon_{\downarrow,\text{tot}} + \epsilon_{\uparrow,\text{tot}}}{2}. \quad (5)$$

In particular, a minimum of $\tilde{\epsilon}$ is obtained for the same values of detection time t_{det} and the threshold on the number of photons n_{th} , as the minimum of ϵ .

4. Experimental sequence

In the experiment, two sets of data are taken. In each set the ion is prepared in one of the two Zeeman qubit states, $|\uparrow\rangle$ or $|\downarrow\rangle$, and then state detection is performed. Each set of data contains 3×10^5 repetitions of the experiment, yielding a statistical uncertainty of the estimated measurement error that is below 1×10^{-4} .

In both sequences the ion is first Doppler cooled on the $S_{1/2} \rightarrow P_{1/2}$ transition for $300 \mu\text{s}$, resulting in a mean axial harmonic oscillator number of $\bar{n} \simeq 25$. Secondly, sideband cooling is performed on the $S_{1/2,+1/2} \rightarrow D_{5/2,+3/2}$ narrow transition. To this end, the red sideband of the $S_{1/2,+1/2} \rightarrow D_{5/2,+3/2}$ transition is continuously excited for 5 ms with the 674 nm laser, while the 1033 nm laser is left on in order to repump the population from the $D_{5/2}$ metastable level, and a σ^+ polarized 422 nm light is left on in order to repump the population from the $S_{1/2,-1/2}$ state via the $P_{1/2}$ manifold. Following sideband cooling the mean axial harmonic oscillator number is $\bar{n} = 0.3(2)$.

Following cooling, the spin state is initialized. At this stage, it is highly probable that the qubit is already in the $|\uparrow\rangle$ state. To increase this probability further, we leave the σ^+ polarized, 422 nm optical pumping beam for an additional $50 \mu\text{s}$. To initialize the qubit in the $|\downarrow\rangle$ state, we use an $8 \mu\text{s}$ coherent qubit rotation to bring the electron from $|\uparrow\rangle$ to $|\downarrow\rangle$. Optical pumping using the 674 nm laser follows, to further increase the initialization efficiency. Ten consecutive π -pulses on the $S_{1/2,\mp 1/2} \rightarrow D_{5/2,\pm 1/2}$ transition, each followed by a 1033 nm repump pulse, pump the remaining population out of the $|\downarrow\rangle$ or $|\uparrow\rangle$ state, respectively.

State detection begins with electron shelving. An $8.5 \mu\text{s}$ -long π -pulse on the $|\uparrow\rangle \rightarrow D_{5/2,+3/2}$ transition is applied. To increase shelving efficiency, another, $14 \mu\text{s}$ -long, π -pulse is applied on the $|\uparrow\rangle \rightarrow D_{5/2,-1/2}$ transition. Following shelving, an on-resonance 422 nm laser light is shined on the ion for $500 \mu\text{s}$, during which fluorescent photons are collected by the

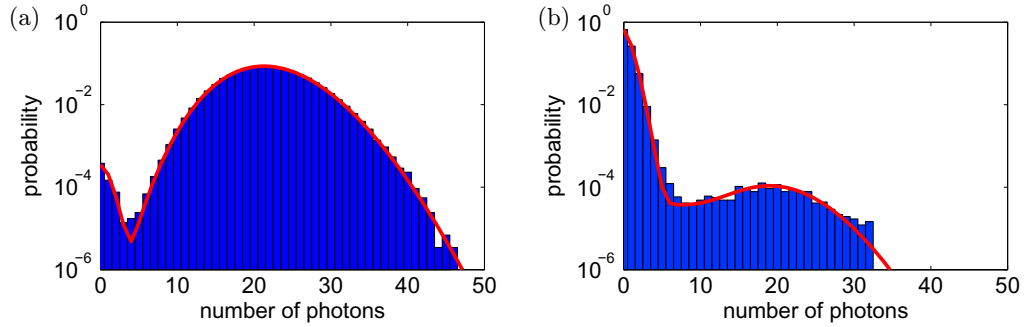


Figure 4. Experimentally obtained PDFs for a detection time of $t_{\text{det}} = 285 \mu\text{s}$. The ion is initialized in the $|\downarrow\rangle$ state in (a) and in the $|\uparrow\rangle$ state in (b). A maximum likelihood fit to the expected distribution functions, given by equations (3a) and (3b), is shown (solid red line). Total initialization and shelving errors for the $|\downarrow\rangle$ and $|\uparrow\rangle$ states obtained from the fit are $\epsilon_{\downarrow} = 6(1) \times 10^{-4}$ and $\epsilon_{\uparrow} = 10(1) \times 10^{-4}$, respectively.

PMT and their time of arrival is recorded for further analysis. Then, any population shelved to the $D_{5/2}$ level is repumped back to the ground state using a $100 \mu\text{s}$ long, 1033 nm laser pulse. At the end of the sequence, a red-detuned 422 nm light Doppler-cools the ion until the next sequence begins. During the entire sequence the 1092 nm laser is left on in order to repump population from the $D_{3/2}$ metastable level.

5. State detection results

Normalized histograms of the number of detected photons that were obtained in the two experiments for $t_{\text{det}} = 285 \mu\text{s}$ are plotted in figures 4(a) and (b). A maximum likelihood fit to the expected distribution functions given by equations (3a) and (3b) is shown by the solid red line. The known detection time $t_{\text{det}} = 285 \mu\text{s}$ and $D_{5/2}$ level lifetime $\tau_{D_{5/2}} = 390 \text{ ms}$ [19] are used, whereas \bar{n}_b , \bar{n}_d , $\epsilon_{\downarrow, \text{tot}}$ and $\epsilon_{\uparrow, \text{tot}}$ are fit parameters. The sum of the initialization and shelving errors for the bright and dark states obtained from the fit is $\epsilon_{\downarrow, \text{tot}} = 6(1) \times 10^{-4}$ and $\epsilon_{\uparrow, \text{tot}} = 10(1) \times 10^{-4}$, respectively.

To determine the minimal detection error and the optimal parameters required to obtain it, we contour plot the measured mean error as a function of the detection time, t_{det} , and the threshold value, n_{th} , in figure 3(b). Here, the mean error resulting from initialization and shelving $\frac{\epsilon_{\downarrow} + \epsilon_{\uparrow}}{2} = 8(1) \times 10^{-4}$ is subtracted. As shown, the experimental plot reproduces the theoretical error plot shown in figure 3(a) relatively well. In particular, the optimal parameters determined experimentally ($t_{\text{det}} = 285 \mu\text{s}$, $n_{\text{th}} = 6$) and the minimal error resulting from imperfect state discrimination $\epsilon = 3(1) \times 10^{-4}$ approach the estimated optimal parameters ($t_{\text{det}} = 280 \mu\text{s}$, $n_{\text{th}} = 5$) and detection error $\epsilon = 2.9 \times 10^{-4}$.

6. Error budget

The error shown in figures 3(a) and (b) is fundamental and does not result from technical imperfections. As shown by Myerson *et al* [4], this error can be somewhat reduced by

Table 1. Shelving and initialization error budget for the two different qubit states. Errors are given in units of 10^{-4} . The initialization error results from off-resonant coupling to the other qubit state. The different error sources in the shelving operation are detailed. The total shelving error for the $|\uparrow\rangle$ state is obtained by summing all shelving error sources in each of the pulses, excluding the contributions of different off-resonance excitations and $D_{5/2}$ level decay. After the two sums are multiplied, the excluded errors are added.

Error source	$ \uparrow\rangle$		$ \downarrow\rangle$	
Initialization				
Coherent off-resonance excitation	1		1	
Incoherent off-resonance excitation	0.5		0.5	
Initialization total error	1.5		1.5	
Shelving				
	1st pulse	2nd pulse	1st pulse	2nd pulse
Coherent off-resonance excitation	–		2	
Incoherent off-resonance excitation	–		1	
Off-resonance sideband excitation	0.5		–	
$D_{5/2}$ level decay during shelving	0.5		–	
Axial motion in the trap	0.1	1	–	
Radial motion in the trap	3	10	–	
Beam pointing noise	30	30	–	
Frequency drift	30	30	–	
Fast laser linewidth	20	20	–	
Magnetic field noise	15	45	–	
Shelving total error	2.5		3	
Overall estimated error	4		4.5	
Overall measured error	10(1)		6(1)	

accounting for the photon times of arrival². Shelving and initialization errors, however, result from technical imperfections. In the following discussion, we try to point out the dominant sources for these errors by calculating an order of magnitude estimates for the contribution of different possible error sources. A summary of this error budget is presented in table 1.

6.1. Initialization error

The first stage of initialization consists of optical pumping to the $|\uparrow\rangle$ state via the $P_{1/2}$ manifold. Ideally, the optical pumping beam has to match a perfect σ^+ polarization. Otherwise, the matrix elements for the $S_{1/2,+1/2} \rightarrow P_{1/2,\pm 1/2}$ transitions will not null, and some population will be pumped out of the $|\uparrow\rangle$ state. To this end, the wave vector, \vec{k} , of the beam has to be exactly parallel to the external magnetic field and a perfect circular polarization is required. We found the fidelity of this initialization step in our setup to be limited to less than 0.999 due to stress-induced birefringence in the fused silica vacuum chamber optical ports.

To increase initialization efficiency, we use the narrow-linewidth 674 nm laser to optically pump the remaining population from the $|\downarrow\rangle$ state to the $|\uparrow\rangle$ state via the $D_{5/2,+1/2}$ level, as

² By similarly analyzing photon arrival times, we were indeed able to lower this error to $2(1) \times 10^{-4}$.

described above. This initialization procedure is limited due to the finite off-resonance excitation probability on the $S_{1/2,+1/2} \rightarrow D_{5/2,+3/2}$ transition, resulting in a finite probability for the electron to be in the $|\downarrow\rangle$ state at the end of the process. Note that there are two different contributions to off-resonant excitation. The first is coherent with respect to the resonant light component and is due to the pulse finite time. The second is incoherent and is due to the servo bumps. In the steady state, i.e. after a sufficient number of pulses, this probability is given by the ratio of the $|\uparrow\rangle \rightarrow |\downarrow\rangle$ and $|\downarrow\rangle \rightarrow |\uparrow\rangle$ transfer probabilities. These are, in turn, estimated based on the off-resonance excitation rate, the polarization of the 1033 nm repump laser and the different decay probabilities from the $P_{3/2}$ excited states to either the $|\uparrow\rangle$ or $|\downarrow\rangle$ states. The incoherent off-resonance excitation rate is directly measured and is seen to be very sensitive to the specific laser and servo-loop working parameters, such as current or gain; we have observed this rate change by a factor of 2 when working with slightly different parameters. The coherent off-resonance excitation rate is estimated based on the measured Rabi frequencies and detuning. We thus estimate the $|\uparrow\rangle$ state initialization error to be $\sim 1 \times 10^{-4}$ due to coherent off-resonance excitation and $\sim 0.5 \times 10^{-4}$ due to incoherent off-resonance excitation.

When initializing to the $|\downarrow\rangle$ state, we initially perform optical pumping to the $|\uparrow\rangle$ state and apply an RF π -pulse, which transfers the electron to the $|\downarrow\rangle$ state with a fidelity higher than 0.999. This procedure is followed by ten similar pulses on the $S_{1/2,+1/2} \rightarrow D_{5/2,-1/2}$ transition, which result in $|\downarrow\rangle$ state initialization with the same error as for the $|\uparrow\rangle$ state.

Note that another possible error in the initialization process could arise from leakage of 422 nm laser light, resulting in the mixing of the two qubit states. This was, however, found not to be a problem in our system by measuring the lifetime of each of the qubit states.

6.2. Electron shelving error

The error in the shelving process is different for the two qubit states and is therefore analyzed separately.

$|\downarrow\rangle$ state shelving error. For the $|\downarrow\rangle$ state, the shelving error is the probability that the ion was shelved to the $D_{5/2}$ level manifold due to off-resonant light. The nearest transition from $|\downarrow\rangle$ to the $D_{5/2}$ level is 5.35 MHz detuned from the laser carrier, and the coupling to the motional sidebands is suppressed by the Lamb–Dicke parameter ($\eta = 0.05$ for the longitudinal motion). Here, the contribution of coherent off-resonance excitations during the two shelving pulses to the error is estimated to be $\sim 2 \times 10^{-4}$, while the error due to incoherent excitations is $\sim 1 \times 10^{-4}$.

$|\uparrow\rangle$ state shelving error. For the $|\uparrow\rangle$ state, the shelving error is the probability that the ion remained in the $S_{1/2}$ manifold after shelving was performed. A number of factors contribute to this error.

The shelving transition Rabi frequency depends on the ions' motion through the Debye–Waller factor. The temperature of the ion therefore has a large effect on the shelving error. The ion is initially Doppler-cooled to a mean axial harmonic oscillator number of $\bar{n} \simeq 25$. This leads to an error of $\simeq 0.01$ in a single shelving π -pulse. It is important to note that in the second shelving pulse the error is increased to $\simeq 0.1$ due to the change in the level occupation distribution induced by the first pulse; following the first pulse, motional states with a smaller Debye–Waller factor are preferentially left at the $S_{1/2}$ level. To reduce this error, Doppler cooling of the ion is followed by sideband cooling on the $S_{1/2,+1/2} \rightarrow D_{5/2,+3/2}$ transition. After 5 ms cooling, a mean axial harmonic oscillator number of $\bar{n} = 0.3(2)$, inferred from the imbalance

between the motional sidebands is reached. However, the mean harmonic oscillator level does not provide the full motional population distribution, which is required to estimate the shelving error. A thermal distribution with $\bar{n} = 0.3$ would lead to a shelving error equal to $\sim 1 \times 10^{-5}$ in the first pulse and $\sim 1 \times 10^{-4}$ in the second. However, the distribution of high-harmonic oscillator levels, following sideband cooling, is poorly described by a thermal distribution. This is because motional states outside the Lamb–Dicke regime have a small Debye–Waller factor on the cooling transition and are therefore not cooled efficiently. The exact dynamics of the sideband cooling process and the resulting energy level distribution are not calculated here. In our estimates, we use the error values assuming a thermal distribution. This is probably an overly optimistic estimate and could be the source of the discrepancy between our evaluated and measured errors for the $|\uparrow\rangle$ state.

Motion along the radial direction of the trap has a much weaker effect on shelving infidelity, because of the stronger confinement along this direction. However, while sideband cooling is performed for the axial motion, the radial motion is only Doppler-cooled and thus cannot be neglected. We estimate the infidelity due to radial motion to be $\sim 3 \times 10^{-4}$ in the first pulse and $\sim 1 \times 10^{-3}$ in the second pulse.

Intensity fluctuations of the 674 nm laser are reduced to a negligible level using an intensity noise eater. An effective residual intensity noise resulting from beam pointing fluctuations on the ion is estimated to give an error of $\sim 3 \times 10^{-3}$ in a single shelving pulse.

Magnetic field fluctuations are studied in a Ramsey experiment on the $|\uparrow\rangle \rightarrow |\downarrow\rangle$ transition, where a coherence time of 500 μs is measured. The resulting errors are estimated by numerical solution of the optical Bloch equations with a corresponding coherence decay term. Taking into account the different magnetic field susceptibilities for the different transitions, as well as the different durations for the two shelving pulses, we estimate the errors to be $\sim 1.5 \times 10^{-3}$ and $\sim 4.5 \times 10^{-3}$ for the two π -pulses, respectively.

A different contribution to the shelving error results from laser frequency noise. As detailed above, this noise has a few spectral contributions. Noises that are slow compared with the experiment time result in a typical laser frequency drift of 2 kHz between consecutive scans of the atomic line, giving a shelving error of $\sim 3 \times 10^{-3}$ per pulse. The contribution of the laser linewidth to the decoherence rate is found in a Ramsey experiment on the $S_{1/2,+1/2} \rightarrow D_{5/2,+3/2}$, yielding a coherence time of 700 μs . After quadratically subtracting the contribution of magnetic field fluctuations to this decoherence rate, we estimate the error owing to the linewidth of the laser alone to be $\sim 2 \times 10^{-3}$ in a single shelving pulse.

The finite decay probability from the $D_{5/2}$ level manifold during the shelving process also contributes to the $|\uparrow\rangle$ state shelving error. This probability has two contributions. The first is due to the finite lifetime of the metastable level $\tau_{D_{5/2}} = 390$ ms [19]. After the first shelving pulse, the electron is found at the $D_{5/2}$ level with high probability and therefore it decays with the rate $\frac{1}{\tau_{D_{5/2}}}$ during the second shelving pulse. During the first shelving pulse this error is half as large, because, on average, only half of the population is in the $D_{5/2}$ manifold. Using pulse durations of 8.5 and 14 μs , we estimate this effect to give a contribution of $\sim 0.5 \times 10^{-4}$ to the shelving error. The second contribution is due to off-resonant coupling of light to motional sidebands. This coupling results in population transfer from the $D_{5/2}$ manifold back to the $|\uparrow\rangle$ state. The largest such contribution is due to the incoherent light in the servo bump, which has a significant spectral overlap with the axial-motion sidebands, located 1.1 MHz away from the carrier. The estimated contribution to the error here is $\sim 0.5 \times 10^{-4}$ for the two shelving pulses combined.

In addition, the leakage of 1033 nm laser light during detection can shorten the lifetime of the $D_{5/2}$ metastable state and thus reduce detection fidelity. In this experiment, we find the lifetime of the $D_{5/2}$ level to be consistent with that reported in [19], indicating that leakage of repump light has no significant effect.

Summing up all the different contributions to the $|\uparrow\rangle$ state shelving error after both π -pulses, we obtain an error estimate equal to $\sim 2.5 \times 10^{-4}$.

6.3. Error summary

A summary of the estimated initialization and shelving errors and their sources is presented in table 1 in units of 10^{-4} . The total estimated errors for the $|\uparrow\rangle$ and $|\downarrow\rangle$ states are $\sim 4 \times 10^{-4}$ and $\sim 4.5 \times 10^{-4}$, respectively, whereas the measured errors of $10(1) \times 10^{-4}$ and $6(1) \times 10^{-4}$, respectively, are roughly twice as large.

As the error budget suggests, one significant source for initialization and shelving errors is off-resonance excitation. This is not surprising considering that here one needs to spectrally distinguish between two states that differ by 13 MHz on top of a 445 THz transition. There are two main contributions to off-resonance excitation. The first is coherent and is due to the pulse finite time, while the second is incoherent and is driven by the laser servo bumps. There are several possible avenues for reducing these errors. Increasing the magnetic field and thus the separation between the qubit states will reduce the off-resonance excitation probability. Decreasing the shelving laser intensity will reduce both coherent and incoherent off-resonance excitation errors. Slowing down the shelving transition Rabi frequency, thereby increasing the pulse length, will reduce the coherent off-resonance excitation error in proportion to the laser intensity. Secondly, since the pulse time is proportional to the square root of the laser intensity, whereas the incoherent off-resonance excitation rate is proportional to the laser intensity, the incoherent off-resonance excitation error will decrease as the intensity square root. Note that this error reduction will come at the expense of larger error contributions due to slower laser frequency noise (drift and linewidth) and magnetic field noise. The shelving laser servo bumps can be reduced by engineering a faster servo system, by using a laser that has a narrower noise bandwidth to begin with (diode laser systems are notorious for their broad-frequency noise spectrum), or by spectral filtering.

Here, incoherent off-resonance excitation errors are below 10^{-3} . However, it is worth noting that this error source becomes much larger when carrying out operations that are off-resonance from the carrier, where the servo bump and the transition carrier have a significant overlap. We observe a large error caused by the servo bump when performing rapid adiabatic passage (RAP) on the $S_{1/2} \rightarrow D_{5/2}$ transition [13], as well as when driving the motional sideband.

As mentioned above, a possible explanation of the discrepancy between the estimated and measured $|\uparrow\rangle$ state errors is a deviation of the ions' harmonic oscillator energy level distribution from a thermal distribution. Such a deviation is not surprising, since in instances in which the ion motion is high both the sideband cooling mechanism and the shelving transition are likely to fail. As an example, starting from a thermal distribution after Doppler cooling, failure to sideband cool all the instances where the ion motion is in $n > 90$ will produce a larger shelving error than we measure. Reducing this error contribution will require better cooling of the tail of the ion energy distribution, via e.g. second-sideband cooling.

7. High-fidelity quantum-state tomography

Ion-qubit state measurement is an important tool for executing many quantum algorithms [20–22] and for studying different quantum processes via state and process tomography [23–25]. In all these cases, the states that are being measured do not necessarily coincide with the electronic eigenbasis (the two Zeeman states in the case of a Zeeman qubit). However, all these states are related to the electronic eigenbasis via single-qubit rotations. Typically, measurement fidelity has been characterized as the average fidelity of state detection for the two electronic eigenstates (which are also the measurement eigenbasis). The fidelity of single-qubit rotations was separately benchmarked [26]. However, the error introduced by rotations is not uniformly spread over all possible input states. To this end, the experimental estimate of state tomography fidelity, averaged over all possible single ion-qubit states, is beneficial.

Qubit state tomography is represented by a quantum map ϵ . The fidelity of state tomography of a given pure input state $\rho_j = |\Psi_j\rangle\langle\Psi_j|$ is therefore the fidelity of this state and the reconstructed output state $\epsilon(\rho_j)$,

$$F = \text{Tr}(\epsilon(\rho_j)\rho_j). \quad (6)$$

The output state $\epsilon(\rho_j)$ is reconstructed by

$$\epsilon(\rho_j) = \frac{1}{2}(I + p_x\sigma_x + p_y\sigma_y + p_z\sigma_z). \quad (7)$$

Here, p_x , p_y and p_z are the measured projections of ρ_j on the x -, y - and z -axes correspondingly and σ_j are the Pauli spin operators [15]. Note that this definition of the fidelity is in agreement with equation (1) for the special cases of $|\Psi_j\rangle = |\downarrow\rangle, |\uparrow\rangle$.

Here, we are interested in determining the fidelity of state tomography averaged over all possible input states. A value for the fidelity, averaged over all possible qubit states, can be obtained by calculating an algebraic average of the fidelities of the six pure input states $|-z\rangle = |\downarrow\rangle$, $|+z\rangle = |\uparrow\rangle$, $|\pm x\rangle = (|\downarrow\rangle \pm |\uparrow\rangle)/\sqrt{2}$ and $|\pm y\rangle = (|\downarrow\rangle \pm i|\uparrow\rangle)/\sqrt{2}$ [28]. These measurements require the ability to initialize the qubit in different states, as well as carry out measurements in different bases. Both are achieved via qubit rotations.

The experimental sequence performed is similar to that discussed previously. Briefly, the ion is first ground-state cooled. Then state preparation is performed; the qubit is first prepared in either the $|+z\rangle$ or $|-z\rangle$ state and, when required, is rotated to initialize the $|\pm x\rangle$, $|\pm y\rangle$ states. Projection measurement consists of mapping the measurement basis onto the $|\pm z\rangle$ basis, once again using qubit rotations, followed by shelving and state-selective fluorescence detection. In principle, a total of 18 measurements, three for each input state, is needed. However, since there is no phase information in the detection process, only nine measurements are not redundant and were therefore carried out. The measurement uncertainties are determined by the quantity of collected statistics. For the projections on an axis that is parallel to the input state, 2×10^5 repetitions were performed, yielding an error of 2×10^{-4} . For projections on an axis that is orthogonal to the input state 1×10^4 repetitions were performed, which yield an uncertainty of 1×10^{-2} . A summary of the different measured projections and the calculated fidelities for different input states is presented in table 2.

The $|\pm z\rangle$ measurement fidelities here are somewhat lower than the best effort presented above. This might be due to slightly non-optimal detection parameters³. The measurement

³ The optimal t_{det} and n_{th} values depend on the photon detection rates, R_b and R_d , which can drift due to small changes in the laser parameters.

Table 2. Summary of the state tomography results. The uncertainties in the values of the projections on axis parallel to the initial state are 2×10^{-4} . For projections on the orthogonal axis the uncertainties are 1×10^{-2} . The uncertainties for the calculated fidelities are presented in the table.

	X projection	Y projection	Z projection	Fidelity
+z	-0.011	-0.011	0.9967	0.9984(2)
-z	0.005	0.005	-0.9975	0.9988(2)
+x	0.9948	0.003	0.005	0.9974(2)
-x	-0.9957	0.017	0.005	0.9979(2)
+y	0.017	0.9948	0.005	0.9974(2)
-y	-0.003	-0.9957	0.005	0.9979(2)
Averaged				0.9979(2)

fidelities for the $|\pm x\rangle$, $|\pm y\rangle$ states are generally lower than the $|\pm z\rangle$ measurement fidelities due to larger state initialization and detection errors caused by imperfect qubit rotations. The non-zero projections in measurement basis orthogonal to the initialization axis are due to systematic errors in the preparation and the measurement sequence (e.g. slightly incorrect pulse durations). Note, however, that all the measured state projections are within two standard deviations of the expected value⁴. Based on the measurements made, we calculate the averaged state tomography fidelity over the entire Bloch sphere to be $\bar{F} = 0.9979(2)$.

A more complete characterization of the detection process is achieved by performing full process tomography [15]. We use the chi matrix, χ , representation to characterize the completely positive map representing the detection process,

$$\epsilon(\rho_j) = \sum_{m,n=1}^4 \chi_{mn} E_m \rho_j E_n^\dagger. \quad (8)$$

Here, the fixed set $\{E_m\}_{m=1}^4 = \{I, \sigma_x, i\sigma_y, \sigma_z\}$ forms a basis for single-qubit quantum maps. Ideally, the detection process would be represented by the chi matrix

$$\chi_{\text{ideal}} = \begin{pmatrix} 1 & 0 & 0 & 0 \\ 0 & 0 & 0 & 0 \\ 0 & 0 & 0 & 0 \\ 0 & 0 & 0 & 0 \end{pmatrix}, \quad (9)$$

corresponding to the Identity operation.

To determine the chi matrix of a single-qubit map experimentally, it is enough to measure the output density matrices for the following set of four, linearly independent, input density matrices, $\{|+z\rangle\langle+z|, |-z\rangle\langle-z|, |+x\rangle\langle+x|, |+y\rangle\langle+y|\}$. An explicit formula can then be obtained for the chi matrix values [15]. The non-zero orthogonal state projections, originating from systematic and statistical errors, result in a non-physical (non-positive) reconstructed chi matrix.

⁴ In fact, taking into account the imbalance in the fidelities of $\pm Z$, the projection on an orthogonal axis is expected to be -2×10^{-4} .

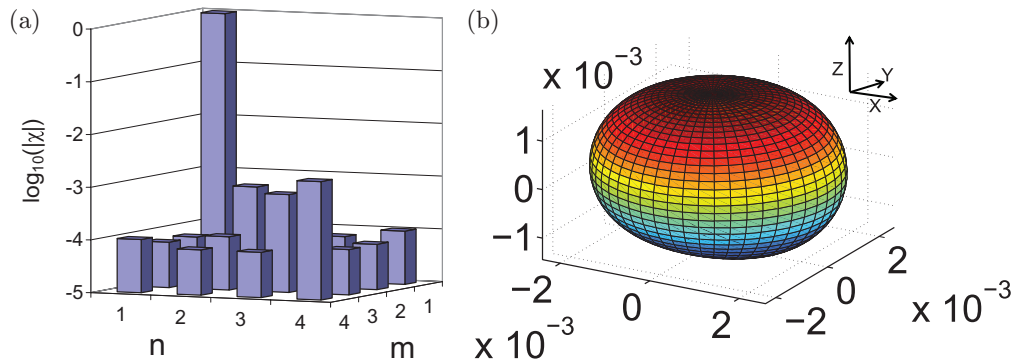


Figure 5. Process tomography results for the detection process. (a) Absolute values of the reconstructed chi matrix entries. (b) Detection error for every pure input state reproduced using the reconstructed chi matrix. Here, the error in detecting the pure state, associated with given azimuthal and polar angles on the Bloch sphere, is represented by the radial distance from the origin of the shown surface in that direction. The resulting spheroid is slightly oblate due to an increased error in the equatorial direction. This additional error is due to imperfections in the RF pulses used to initialize qubit superpositions.

To obtain a meaningful physical chi matrix, we therefore null all orthogonal state projections⁵. The absolute values of the reconstructed chi matrix entries are plotted in figure 5(a) on a logarithmic scale. As expected, χ_{11} , which represents the identity operation, is three orders of magnitude larger than any other entry. Other diagonal entries are an order of magnitude larger than off-diagonal entries, implying that qubit depolarization is the main error channel. The increased measurement error of superposition states, due to rotation errors, is manifested in the slightly larger χ_{44} (dephasing channel) as compared with χ_{22} and χ_{33} (spin-flip channels). Off-diagonal elements are due to the small imbalance between the measurement fidelity of the $|+z\rangle$ and the $|-z\rangle$ states.

Using the obtained chi matrix, one can calculate the output of any input state, and hence also the fidelity. Figure 5 depicts the detection error over the entire Bloch sphere. The polar angle, θ , and the azimuthal angle, ϕ , define the pure state $|\Psi\rangle = \cos(\frac{\theta}{2})|\uparrow\rangle + e^{i\phi} \sin(\frac{\theta}{2})|\downarrow\rangle$, whereas the radial distance from the origin in this direction indicates the error for this state. As expected from qubit depolarization, an almost spherical spheroid is obtained. The resulting spheroid is also somewhat oblate due to the added error in qubit rotations and is minutely dilated in the positive hemisphere direction, owing to the slight imbalance between the measurement fidelity of the $|+z\rangle$ and $|-z\rangle$ states. Using the reconstructed chi matrix, we find the process fidelity to be $F_{\text{proc}} = \text{Tr}(\chi_{\text{ideal}} \chi_{\text{proc}}) = 0.997(1)$.

⁵ A different approach would have been to perform a maximum likelihood estimate of a physical operation [25, 27]. However, since we believe that we have identified the origin of the operation non-positiveness with the small finite projection in the orthogonal direction, the better approach, in our opinion, is to null those. Two more notes: with better statistics the magnitude of orthogonal projections can be increasingly lowered by adjusting the rotation pulse time; and by artificially nulling these projections the estimate of the error becomes larger and is therefore pessimistic.

8. Summary

In conclusion, we demonstrated high-fidelity state detection of a qubit encoded in the Zeeman splitting of the ground state of a single $^{88}\text{Sr}^+$ ion. The limitations of the best effort readout fidelity of 0.9989(1) were analyzed in detail. Our estimate of the contribution of imperfect state preparation and shelving to the measured error is $\sim 8 \times 10^{-4}$. The remaining part, $\sim 3 \times 10^{-4}$, results from limited state discrimination efficiency owing to the finite lifetime of the metastable level. This fraction of the error is intrinsic to our state detection scheme, and can be somewhat decreased if the information on photon detection times is used [4].

Since one of the applications of high-fidelity state detection is performing high-accuracy quantum process tomography, we measured the averaged state tomography fidelity over the entire Bloch sphere, which is 0.9979(2). We also performed quantum process tomography for the detection process, and found the process fidelity to be $F_{\text{proc}} = 0.997(1)$. This fidelity can be further increased if higher-fidelity qubit rotations are used.

Our measured state detection fidelity is compatible with recent estimates of the required fault-tolerance error threshold and can be used in future to implement effective quantum error correction protocols. In addition, highly accurate quantum process tomography, important for the study of basic quantum processes, can be implemented.

Acknowledgments

We gratefully acknowledge support from the ISF Morasha program, the Crown Photonics Center and the Minerva Foundation.

References

- [1] DiVincenzo D P 2000 The physical implementation of quantum computation *Fortschr. Phys.* **48** 771
- [2] Knill E 2005 Quantum computing with realistically noisy devices *Nature* **434** 39
- [3] Wineland D J *et al* 1998 Experimental issues in coherent quantum-state manipulation of trapped atomic ions *J. Res. Natl Inst. Stand. Technol.* **103** 259
- [4] Myerson A H *et al* 2008 High-fidelity readout of trapped-ion qubits *Phys. Rev. Lett.* **100** 200502
- [5] Burrell A H, Szwer D J, Webster S C and Lucas D M 2010 Scalable simultaneous multiqubit readout with 99.99% single-shot fidelity *Phys. Rev. A* **81** 040302
- [6] Hume D B, Rosenband T and Wineland D J 2007 High-fidelity adaptive qubit detection through repetitive quantum nondemolition measurements *Phys. Rev. Lett.* **99** 120502
- [7] Langer C *et al* 2005 Long-lived qubit memory using atomic ions *Phys. Rev. Lett.* **95** 60502
- [8] Acton M, Brickman K A, Haljan P C, Lee P J, Deslauriers L and Monroe C 2006 Near-perfect simultaneous measurement of a qubit register *Quantum Inf. Comp.* **6** 465
- [9] Langer C E 2006 High fidelity quantum information processing with trapped ions *PhD Thesis* University of Colorado http://tf.nist.gov/ion/qucomp/papers/clthesis/langer_phdthesis.pdf
- [10] Olmschenk S, Younge K C, Moehring D L, Matsukevich D N, Maunz P and Monroe C 2007 Manipulation and detection of a trapped Yb^+ hyperfine qubit *Phys. Rev. A* **76** 052314
- [11] Schaetz T *et al* 2005 Enhanced quantum state detection efficiency through quantum information processing *Phys. Rev. Lett.* **94** 010501
- [12] McDonnell M J *et al* 2004 High-efficiency detection of a single quantum of angular momentum by suppression of optical pumping *Phys. Rev. Lett.* **93** 153601
- [13] Wunderlich C 2007 Robust state preparation of a single trapped ion by adiabatic passage *J. Mod. Opt.* **54** 1541

- [14] Poschinger U G *et al* 2009 Coherent manipulation of a $^{40}\text{Ca}^+$ spin qubit in a micro ion trap *J Phys. B: At. Mol. Opt. Phys.* B **42** 154013
- [15] Nielsen M A and Chuang I L 2000 *Quantum Computation and Quantum Information* (Cambridge: Cambridge University Press)
- [16] Sengstock K, Sterr U, Müller J H, Rieger V, Bettermann D and Ertmer W 1994 Optical Ramsey spectroscopy on laser-trapped and thermal Mg atoms *Appl. Phys. B* **59** 99
- [17] Glickman Y *et al* in preparation
- [18] Keselman A 2010 High fidelity ion qubit state detection *MSc Thesis* Feinberg Graduate School, Weizmann Institute of Science http://www.weizmann.ac.il/complex/ozeri/uploads/AK_thesis.pdf
- [19] Letchumanan V, Wilson M A, Gill P and Sinclair A G 2005 Lifetime measurement of the metastable $4d^2D_{5/2}$ state in $^{88}\text{Sr}^+$ using a single trapped ion *Phys. Rev. A* **72** 12509
- [20] Barrett M D *et al* 2004 Deterministic quantum teleportation of atomic qubits *Nature* **429** 737
- [21] Riebe M *et al* 2004 Deterministic quantum teleportation with atoms *Nature* **429** 734
- [22] Chiaverini J *et al* 2004 Realization of quantum error correction *Nature* **432** 602
- [23] Riebe M *et al* 2006 Process tomography of ion trap quantum gates *Phys. Rev. Lett.* **97** 220407
- [24] Riebe M *et al* 2007 Teleportation with atoms: quantum process tomography *New J. Phys.* **9** 211
- [25] Hannemann T, Wunderlich C, Plesch M, Ziman M and Buzek V 2009 Scrutinizing single-qubit quantum channels: theory and experiment with trapped ions arXiv:0904.0923
- [26] Knill E *et al* 2008 Randomized benchmarking of quantum gates *Phys. Rev. A* **77** 012307
- [27] Ziman M, Plesch M, Bužek V and Štelmachovič P 2005 Process reconstruction: from unphysical to physical maps via maximum likelihood *Phys. Rev. A* **72** 022106
- [28] Bowdrey M D, Oi D K L, Short A J, Banaszek K and Jones J A 2002 Fidelity of single qubit maps *Phys. Lett. A* **294** 258